Proton-coupled electron transfer at SOFC electrodes

Citation: J. Chem. Phys. 158, 244107 (2023)

As Published: 10.1063/5.0145247

Publisher: AIP Publishing

Persistent URL: https://hdl.handle.net/1721.1/157438

Version: Final published version: final published article, as it appeared in a journal, conference proceedings, or other formally published context

The Journal of Chemical Physics

RESEARCH ARTICLE | JUNE 23 2023

Proton-coupled electron transfer at SOFC electrodes

Nicholas J. Williams ; Robert E. Warburton ; Ieuan D. Seymour ; Alexander E. Cohen ; Martin Z. Bazant ; Stephen J. Skinner

J. Chem. Phys. 158, 244107 (2023)
https://doi.org/10.1063/5.0145247

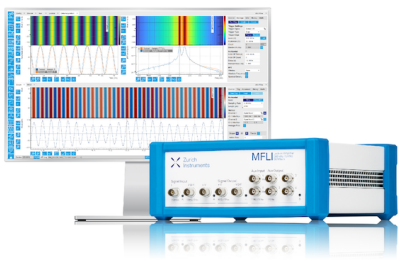

AIP Publishing

The Journal of Chemical Physics ARTICLE scitation.org/journal/jcp

Proton-coupled electron transfer at SOFC electrodes

Cite as: J. Chem. Phys. 158, 244107 (2023); doi: 10.1063/5.0145247
Submitted: 4 February 2023 • Accepted: 30 May 2023 •
Published Online: 23 June 2023

Nicholas J. Williams,[1,2,a] Robert E. Warburton,[3] Ieuan D. Seymour,[1] Alexander E. Cohen,[2] Martin Z. Bazant,[2,4] and Stephen J. Skinner[1]

AFFILIATIONS

[1] Department of Materials, Imperial College London, Exhibition Road, London SW7 2AZ, United Kingdom
[2] Department of Chemical Engineering, Massachusetts Institute of Technology, Cambridge, Massachusetts 02139, USA
[3] Department of Chemical and Biomolecular Engineering, Case Western Reserve University, Cleveland, Ohio 44106, USA
[4] Department of Mathematics, Massachusetts Institute of Technology, 77 Massachusetts Avenue, Cambridge, Massachusetts 02139, USA

[a] Author to whom correspondence should be addressed: nw7g140@gmail.com

ABSTRACT

Understanding the charge transfer processes at solid oxide fuel cell (SOFC) electrodes is critical to designing more efficient and robust materials. Activation losses at SOFC electrodes have been widely attributed to the ambipolar migration of charges at the mixed ionic–electronic conductor–gas interface. Empirical Butler–Volmer kinetics based on the transition state theory is often used to model the current–voltage relationship, where charged particles transfer classically over an energy barrier. However, the hydrogen oxidation/water electrolysis reaction $H_{2(g)} + O^{2-} \rightleftharpoons H_2O_{(g)} + 2e^-$ must be modeled through concerted electron and proton tunneling events, where we unify the theory of the electrostatic surface potential with proton-coupled electron transfer kinetics. We derive a framework for the reaction rate that depends on the electrostatic surface potential, adsorbate dipole moment, the electronic structure of the electron donor/acceptor, and vibronic states of the hydrogen species. This theory was used to study the current–voltage characteristics of the Ni/gadolinium-doped ceria electrode in $H_2/H_2O(g)$, where we find excellent validation of this novel model. These results yield the first reported quantification of the solvent reorganization energy for an SOFC material and suggest that the three-phase boundary mechanism is the dominant pathway for charge transfer at cermet electrodes.

I. INTRODUCTION

The solid oxide fuel cell (SOFC) is a highly efficient chemical-to-electrical energy conversion technology compatible with both existing fuel (e.g., natural gas) and future fuel (e.g., renewably sourced hydrogen) infrastructures.[1–3] These devices work through electrochemical RedOx reactions at the air and fuel electrodes, whereby chemical energy is used to drive external work. The Faradaic reactions at the fuel electrode can be given simply as $H_{2(g)} + O^{2-} \rightleftharpoons H_2O_{(g)} + 2e^-$ (elementary steps are listed in Table I).[4,5] The hydrogen oxidation/water hydrolysis reaction may occur via the two-phase boundary (2 PB) [Fig. 1(a)] or the three-phase boundary (3 PB) [Fig. 1(b)]. At the 2 PB, two neighboring polarons in the CeO_2 surface will combine with two neighboring protons. This process is driven by a combination of the electrostatic potential and the concentration of electronic defects at the interface between mixed ionic–electronic conductors (MIEC) and the gas phase.[2] Alternatively, in the presence of an electrocatalytic metallic phase, the electron–proton recombination may occur via a 3 PB mechanism. Electron density migrates from a polaronic state in the oxide phase to the metal; meanwhile, the proton is reduced as it migrates to the metal surface. The electrostatic nature of the 3 PB process is less well studied.

Gadolinium-doped ceria (CGO) displays considerably fast oxygen transport kinetics and high electronic conductivity under reducing conditions.[11–15] To enhance the overall electronic conductivity of the electrode and to increase the density of reactive 3 PB, it is beneficial to mix a metallic phase with the MIEC to create a cermet

TABLE I. Elementary steps for the two-phase boundary (2 PB) and three-phase boundary (3 PB) reaction mechanisms written in the Kröger–Vink notation. For water adsorption, $H_2O_{(g)}$ consumes an oxygen vacancy ($V_O^{\cdot\cdot}$) and an oxygen site (O_O^x), forming two hydroxyls ($OH_O^{\cdot}$) on the CGO surface. This is followed by the rate limiting PCET step. At the 2 PB, two hydroxyls and two polarons (Ce_{Ce}') form $H_{2(g)}$ at the surface of the MIEC. At the 3 PB, one hydroxyl and one polaron combine at a free site on the nickel surface ($*$), forming an adsorbed hydrogen on the nickel surface (H_{Ni}). At the 3 PB, there is an additional hydrogen desorption step.

Elementary step	Two-phase boundary	Three-phase boundary
Water adsorption	$H_2O_{(g)} + V_O^{\cdot\cdot} + O_O^x \rightleftharpoons 2OH_O^{\cdot}$	$H_2O_{(g)} + V_O^{\cdot\cdot} + O_O^x \rightleftharpoons 2OH_O^{\cdot}$
PCET	$2OH_O^{\cdot} + 2Ce_{Ce}' \rightleftharpoons H_{2(g)} + 2O_O^x + 2Ce_{Ce}^x$	$OH_O^{\cdot} + Ce_{Ce}' + * \rightleftharpoons H_{Ni} + O_O^x + +Ce_{Ce}^x$
Hydrogen desorption		$2H_{Ni} \rightleftharpoons H_{2(g)} + 2^*$

electrode, i.e., nickel/gadolinium-doped ceria (Ni/CGO).[1,2,6,16–19] The operation of the Ni/CGO electrode under electrical bias has been studied for decades; however, a unifying model for hydrogen electro-oxidation or water electrolysis has not yet been agreed upon.[18,20–30] Most charge transfer models utilize the empirical Butler–Volmer equation, which is convenient for fitting current–voltage data at low overpotentials.[31,32] However, the Butler–Volmer equation suggests that the electrostatic potential driving the charge transfer reaction is located at the electrode–electrolyte interface. In our previous work, we have illustrated that the electrostatic potential modulated by the state of the electrode is located at the surface of the MIEC.[1,2] The driving force for charge transfer should therefore be determined by the electrostatic potential at the MIEC–gas interface.

Herein, we build on these previous findings to model the kinetics of electron and proton transfer at MIEC–gas interfaces. By accounting for nuclear quantum effects of the transferring proton, the charge transfer at SOFC electrodes can be described within a concerted proton-coupled electron transfer (PCET) framework. Therefore, in this study, we aim to combine the theory of the electrostatic surface potential with the vibronically nonadiabatic PCET theory to develop a unifying kinetic model for charge transfer at MIEC–gas interfaces.[1,2,33–36] This model is adapted to both 2 PB and 3 PB rate expressions that are fit to experimental data to discern the PCET mechanism at MIEC–gas interfaces.

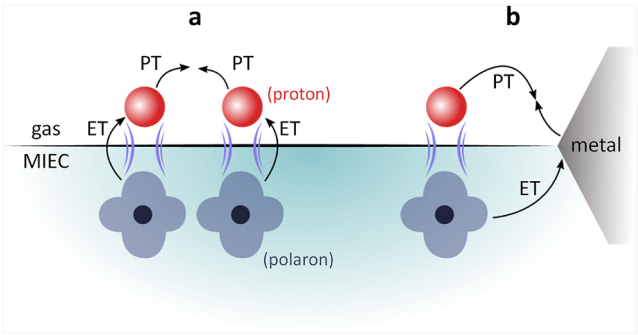

FIG. 1. Schematic illustration of the charge transfer step of the water hydrolysis reaction at the Ni/CGO surface. (a) Via 2 PB pathway, where two protons and two polarons combine at the surface of the MIEC. (b) 3 PB pathway, where the polaron migrates into the metal phase and the proton is reduced at the metal surface forming a neutral hydrogen state. Red spheres and purple isosurfaces represent protons and polarons, respectively. The purple lines represent the electric field created by the intrinsic dipole moment of the surface hydroxyl. PT and ET represent proton transfer and electron transfer processes, respectively.

II. THEORY

A. Thermodynamics

The (electro)chemical potential, μ_i, of a mobile species in an electrochemical system is expressed as[32]

$$\mu_i = \mu_i^{\ominus} + k_B T \ln a_i + z_i e \phi_i = \mu_i^{ex} + k_B T \ln c_i, \tag{1}$$

where $\mu_i^{\ominus}$ is the standard chemical potential, $k_B T \ln a_i$ is the activity potential, and ϕ_i is the electric potential. The activity ($a_i = \gamma_i c_i$) is the product of the concentration (c_i) and activity coefficient (γ_i), which is a measure of the non-ideality of the species.[37,38] A simplification can be made to express all the non-idealities within the excess chemical potential, μ_i^{ex}, which also includes contributions from the standard and electric potentials. Here, we use the definition of (electro)chemical potential, meaning that if the species of interest is charged, we find the electrochemical potential, and if the species of interest is neutral, we find the chemical potential.

As current is drawn, resistances act by changing the cell voltage, V, this departure from the open circuit voltage, V_0, is described as the reservoir chemical potential, $\mu_{res} = e(V_0 - V)$.[32,39–42] The difference between the internally controlled potential (μ_h) and the externally controlled potential (μ_{res}) is given by the reaction affinity, $A_{r,o} = \mu_{res} - \mu_h$, which controls the driving force of absorption of the species from the reservoir. In the case of electrochemical RedOx reactions, the affinity can also be expressed as the activation overpotential (η),[32,39,42]

$$A_{r,o} = ne\eta, \tag{2}$$

where n is the number of electrons transferred in the Faradaic reaction.[43] If we consider the reduction reaction $O^{n+} + ne^- \rightarrow R$, the activation overpotential is described,

$$ne\eta = \mu_R - \mu_O - n\mu_e, \tag{3}$$

where μ_R, μ_O, and μ_e represent the (electro)chemical potentials for the reduced, oxidized, and free electron states, respectively. We can use Eq. (1) to expand Eq. (3) to give the standard electrode potential (E^0), activity, and electrostatic potential,

$$ne\eta = neE^0 + k_B T \ln\left(\frac{a_R}{a_O a_e^n}\right) + z_R e\phi_R - z_O e\phi_O. \tag{4}$$

For electrochemical gas reduction at the SOFC electrodes, the reaction mechanism is often split into multiple steps,

$$\text{net result of steps preceding RDS: } O^{n+} \rightleftharpoons O_{ad}^{n+}, \tag{5}$$

$$\text{RDS: } O_{ad}^{n+} + ne^- \rightleftharpoons R_{ad}, \tag{6}$$

$$\text{net result of steps proceeding RDS: } R_{ad} \rightleftharpoons R, \tag{7}$$

where O_{ad}^{n+} and R_{ad} are the adsorbed states preceding and proceeding the rate determining charge transfer reaction, respectively. To derive the electrostatic surface potential, we assume that the rate determining step of the model system is the transfer of a single electronic charge, $O_{ad}^{+} + e^- \rightarrow R_{ad}$. As such, the activation overpotential is given as (derivation given in the supplementary material)

$$e\eta = \mu_{R_{ad}} - \mu_{O_{ad}} - \mu_e = eE_{rds}^0 + k_B T \ln\left(\frac{a_{R_{ad}}}{a_{O_{ad}} a_e}\right) + e\chi, \tag{8}$$

where E_{rds}^0 is the standard potential of the rate determining (charge transfer) step and χ represents the electrostatic surface potential, which is an electric field formed by the difference in electrostatic potential of the electrode (ϕ_e) and the charged adsorbate (ϕ_{ad}),[1,16,33]

$$\chi = \phi_e - \phi_{ad}. \tag{9}$$

Under bias, an electrostatic potential shift is defined at the surface,

$$\Delta\chi = \chi - \chi^{gas-eq}, \tag{10}$$

where an effective electrical double layer is formed between the electrode surface and the adsorbed species.[44] The notation χ^{gas-eq} refers to the surface potential when the RDS and therefore the electrode surface is in equilibrium with the gas phase and is expressed by the standard potential of the RDS and the activity at equilibrium,[1]

$$\chi^{gas-eq} = -E_{rds}^0 + \frac{k_B T}{e} \ln\left(\frac{a_{O_{ad}}^{gas-eq} a_e^{gas-eq}}{a_{R_{ad}}^{gas-eq}}\right). \tag{11}$$

We must note that at the MIEC–gas interface, applying an activation overpotential departs the electrode surface from equilibrium with the gas phase by changing the concentration of chemical species as well as the magnitude of the electrostatic surface potential.[16,45,46] This key finding is routed in the mechanism by which the electrostatic surface potential is formed, whereby an adsorbate must form on the surface for an electrostatic surface potential to be induced; thus, the coverage of adsorbates on MIEC surfaces is a function of the activation overpotential.[33] Fleig theorized that the origin of the electrostatic surface potential was the dipole moment of the adsorbed gas, $\chi = \vec{\mu}_\perp \rho_0 c_{O_{ad}}/\varepsilon_0$, where $\vec{\mu}_\perp$, ε_0, and ρ_0 represent the dipole moment normal to the surface, vacuum permittivity, and the density of adsorption sites, respectively. This theory was later confirmed by Williams *et al.* by illustrating excellent correlation between the magnitude of the electrostatic surface potential and the intrinsic dipole moment using the density functional theory.[1] By combining Eqs. (8), (10), and (11), we may relate the chemistry of the MIEC–gas interface with the activation overpotential,

$$e\eta = k_B T \ln\left(\frac{c_{R_{ad}}}{c_{O_{ad}} c_e} \frac{c_{O_{ad}}^{gas-eq} c_e^{gas-eq}}{c_{R_{ad}}^{gas-eq}}\right) + e\Delta\chi, \tag{12}$$

where the activity coefficients cancel and the activation overpotential can be expressed in terms of concentration and electrostatic surface potential (derivation in the supplementary material).

B. Electrode kinetics

For SOFC systems, electrode kinetics are often limited by ion or electron transfer events.[32,39,42,47] The overall reaction rate can be written in terms of elementary processes as

$$R_{r,o} = R_r - R_o, \tag{13}$$

where R_r and R_o represent reduction and oxidation rates, respectively. In the framework of nonlinear kinetics, we introduce terms that describe the probability of finding a particle in the desired location, the probability of occupation of the transition state, and the probability of a successful tunneling event once the transition state is occupied. The rate of electrochemical reactions is often described by the phenomenological Butler–Volmer equation, which was originally derived based on the transition state theory to model the rate of ion transfer (IT).[1,32,39,47–49] Here, the rate of ion migration over an activation barrier is determined through classical statistical thermodynamics composed of an attempt frequency and a success probability determined by the thermal energy of the system. The rate for a reduction reaction per surface site for the forward and backward reactions is therefore[32]

$$R_{r,o} = k_0 (c_O c_e)^{1-\alpha} c_R^{\alpha} \left[\exp\left(\frac{-\alpha ne\eta}{k_B T}\right) - \exp\left(\frac{(1-\alpha) ne\eta}{k_B T}\right)\right], \tag{14}$$

where α is the charge transfer coefficient $0 < \alpha < 1$ and k_0 is an overall pre-factor related to the curvatures of the excess free energy landscape near the initial, final, and transition states.[32] By moving the concentration terms outside of the exponent,

$$R_{r,o} = k_0 (c_O c_e)^{1-\alpha} c_R^{\alpha} \left[c_O \exp\left(\frac{-\alpha ne\eta_f}{k_B T}\right) - c_R \exp\left(\frac{(1-\alpha) ne\eta_f}{k_B T}\right)\right], \tag{15}$$

where the formal overpotential reads[38,39,50]

$$ne\eta_f = \mu_R^{ex} - \mu_O^{ex} - n\mu_e = ne\eta + k_B T \ln \frac{c_O}{c_R}, \quad (16)$$

which is a measure of the departure of the electrode potential from the formal one $\eta_f = E^{0\prime} - E$, where $E^{0\prime}$ is the formal electrode potential and E is the applied electrode potential.[38,39]

C. Electron transfer

Tunneling is manifested in quantum mechanics whereby small particles may penetrate a potential energy barrier, resulting in an electron or proton transfer event. The Marcus theory explicitly describes electron transfer (ET) as a tunneling event, which occurs when the reduced and oxidized states are isoenergetic along a collective solvent coordinate.[51,52] The activation energy barrier is determined by the reorganization energy (λ) of the solute and the surrounding solvent environment during charge transfer.[53,54] The forward and backward rates for outer-sphere electron transfer under the framework of the Marcus theory is given,[32,55]

$$R_r(\eta) = k_0^* c_O \exp\left(-\frac{(\lambda + e\eta_f)^2}{4\lambda k_B T}\right), \quad (17)$$

$$R_o(\eta) = k_0^* c_R \exp\left(-\frac{(\lambda - e\eta_f)^2}{4\lambda k_B T}\right), \quad (18)$$

where $k_0^* = k_0 k_T e^{-g_{r,o}/k_B T}$ in which k_T is the electron tunneling probability and $g_{r,o}$ is the work required to bring RedOx species to the reaction site.[39]

In the case where ET involves a metallic phase, the rate is obtained by integrating over all energy levels (ε) in the electrode,[50]

$$R_{r,o}(\varepsilon,\eta) = \int_{-\infty}^{\infty} (R_{r,\varepsilon}(\varepsilon,\eta) - R_{o,\varepsilon}(\varepsilon,\eta))\rho(\varepsilon)d\varepsilon, \quad (19)$$

where $R_{r,\varepsilon}$ and $R_{o,\varepsilon}$ represent the reaction rate dependent on the position of the energy level ε for the forward and backward reactions, respectively, and $\rho(\varepsilon)$ represents the density of electronic states in the electrode.[39,50,56,57] Equation (19) describes electron transfer involving a continuum of states in a metallic electrode by integrating over the energy levels in the electrode. This integral is often described in the literature as the Marcus–Hush–Chidsey theory; however, Dogonadze and Kuznetsov also made pioneering contributions to the nonadiabatic ET theory.[58,59] In general, the tunneling probabilities k_T depend on ε and are a function of the electronic coupling between single-electron states in the metal and the molecular orbitals of the RedOx species.[59,60] However, most theoretical treatments use a coupling matrix element associated with the entire metal d-band as in the Newns–Anderson model and the d-band theory of Hammer and Nørskov.[61] By neglecting variation in the density of states for a metallic electrode, we arrive at the electron transfer rate dependent on the position of the energy level ε for the forward and backward reactions,[55]

$$R_{r,\varepsilon}(\varepsilon,\eta) = k_0^* c_O \exp\left(-\frac{(\lambda + e\eta_f - (\varepsilon - E_F))^2}{4\lambda k_B T}\right) f(\varepsilon), \quad (20)$$

$$R_{o,\varepsilon}(\varepsilon,\eta) = k_0^* c_R \exp\left(-\frac{(\lambda - e\eta_f + (\varepsilon - E_F))^2}{4\lambda k_B T}\right)(1 - f(\varepsilon)). \quad (21)$$

In the above equations, $f(\varepsilon)$ represents Fermi distribution function. Substituting Eqs. (20) and (21) into Eq. (19) yields an improper integral that is not ideal for numerical calculations. As such, Zeng *et al.* derived a uniformly valid analytical approximation for the integrals by matching asymptotic approximations for large and small lambda,[39,59,63]

$$R_r(\eta) = \frac{k_0^* c_O}{1 + e^{\tilde{\eta}_f}} \times \mathrm{erfc}\left(\frac{\tilde{\lambda} - \sqrt{1 + \tilde{\lambda} + \tilde{\eta}_f^2}}{2\sqrt{\tilde{\lambda}}}\right), \quad (22)$$

$$R_o(\eta) = \frac{k_0^* c_R}{1 + e^{-\tilde{\eta}_f}} \times \mathrm{erfc}\left(\frac{\tilde{\lambda} - \sqrt{1 + \tilde{\lambda} + \tilde{\eta}_f^2}}{2\sqrt{\tilde{\lambda}}}\right), \quad (23)$$

where $\tilde{\lambda} = \lambda/k_B T$ and $\tilde{\eta}_f = e\eta/k_B T + \ln(c_O/c_R)$. For the cases for outer-sphere reactions, the relative error of this approximation was calculated to be less than 5% for small overpotentials and negligible for large positive or negative overpotentials.[56]

III. PROTON-COUPLED ELECTRON TRANSFER

By treating the proton quantum mechanically, we derive an expression for rates at the MIEC–gas interface in the framework of proton-coupled electron transfer (PCET). We will begin this section by summarizing the general theory of PCET through the derivation of vibronic states and charge transfer mechanisms. After which, we will look at where PCET is applied to electrochemistry specifically before integrating PCET into the framework of the MIEC–gas interface.

A. Fundamental concepts of PCET theory

PCET reactions are prevalent in many biological, chemical, and electrochemical processes.[34–37,57,62–70] A general reaction square scheme for heterogeneous electrochemical PCET involving the transfer of one electron and one proton is illustrated in Figs. 2(a)–2(c).[67] Because the transferring electron and proton are treated quantum mechanically within this theoretical treatment, such a PCET reaction can be described in terms of the four diabatic states shown on the corners of the surface. As Figs. 2(a)–2(c) imply, the net PCET mechanism could be sequential with initial electron transfer (ET) or proton transfer (PT) producing a thermodynamically stable intermediate, or concerted, without forming such an intermediate.[57]

In the vibronically nonadiabatic PCET theory, the transferring proton and electron are treated quantum mechanically, where the states involved in PCET are mixed electron–proton vibronic states. The vibronic states are a direct product of the initial and final electronic states and proton vibrational states.[34,57] PCET is related to the Marcus theory in that reactive electron–proton tunneling transitions can occur when the free energies of pairs of initial and final vibronic states become degenerate due to polarization of the solvent environment.[32,35,55,71] The center panel of Fig. 2(d) shows a schematic of the Marcus parabolas that represent the free energies

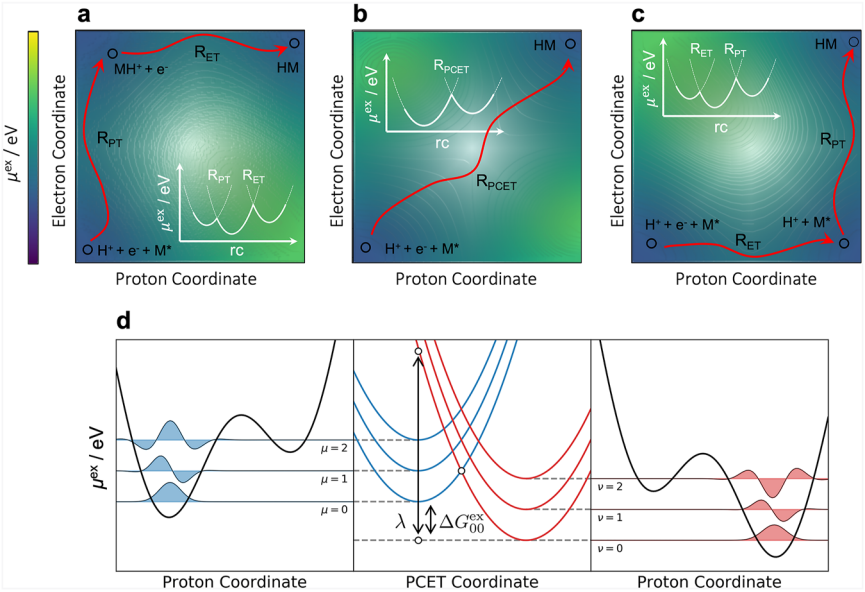

FIG. 2. (a)–(c), Reaction scheme illustrating the heterogeneous proton-coupled electron transfer process, where the electrode participates directly in forming and breaking chemical bonds. H^+, e^-, and M^* represent a proton, electron, and free metal electrode surface site, respectively, H represents the hydrogen atom, MH^+ represents a proton adsorbed onto the metal surface, and MH represents a hydrogen adsorbed onto the metal surface. The contour map details the excess chemical potential energy landscape for (a) ET limited reduction, (b) PCET limited reduction, and (c) PT limited reduction. The planes represent the ET reaction coordinates and the PT reaction coordinate.[39] The axis in white plots represent the 1D chemical potential landscape explored by overall PCET reaction. R_{ET} is the electron transfer (ET) step, R_{PT} is the PT step, and R_{PCET} is the PCET step. (d) Schematic illustration of the excess chemical potential landscape explored by the PCET process. The left-hand panel illustrates the reactant proton potential with its corresponding proton vibrational wave functions along the proton coordinate, while the right-hand panel illustrates the product proton potential with its corresponding proton vibrational wave functions. The middle panel shows a set of stacked PCET Marcus parabolas corresponding to the oxidized (blue) and reduced (red) diabatic states of the reaction. The splitting between the stacked free energy curves corresponds to energy level splitting between the sets of reactant and product vibronic states (μ and ν, respectively). ΔG_{00}^{ex} represents the excess free energy difference between the ground vibronic states of the reactants and products, and λ represents the reorganization energy.

of the initial (blue) and final (red) diabatic states along the collective solvent coordinate for concerted PCET. The probability of a PCET event occurring is proportional to the square of the vibronic coupling matrix ($V_{\mu\nu}$).[35,62,63] This coupling is defined as the Hamiltonian matrix element between the reactant and product vibronic wave functions.[57] In the high temperature regime, the quantum descriptions for the population distributions breakdown to the classical Boltzmann distribution function.[72] The Boltzmann population of vibronic state μ is determined by the temperature and the splitting between μ and the ground state at $\mu = 0$,

$$P_\mu = \frac{e^{-\varepsilon_\mu/k_B T}}{Z}, \tag{24}$$

where Z is the canonical partition function, which normalizes the exponential term,

$$Z = \sum_{\mu=0} e^{-\varepsilon_\mu/k_B T}. \tag{25}$$

As a result of this constant, the probability of all accessible states adds up to one.

B. PCET at electrochemical interfaces

The derivation of PCET applied to electrochemical interfaces given here is similar to the coupled-ion electron transfer (CIET) theory by Fraggedakis *et al.*[39] and follows the same framework combining nonequilibrium thermodynamics with the Marcus theory given by Bazant.[32] The key difference being that ion transfer is treated classically in CIET while proton transfer is also quantum mechanical in PCET. For inner sphere (or heterogeneous) electrochemical PCET, the electrode not only serves as a reservoir for electrons but also participates in chemical bonding.[67] For a metallic electrode in solution, the free energy of reduction ($\Delta G_{\mu\nu}$) for the pair of reactant and product vibronic states μ and ν is the free energy difference between the minima of the corresponding electron–proton vibronic surfaces plus additional terms depending on the electrostatic potentials in solution and in the metal electrode as well as the energy level of the transferring electron in the electrode,[35,67,73]

$$\Delta G_{\mu\nu}(\varepsilon, \eta) = \Delta\varepsilon_{\mu\nu} + k_B T \ln \frac{a_R}{a_O a_e} + z_R e\phi_R - z_O e\phi_O - (\varepsilon - E_F), \tag{26}$$

where $\Delta\varepsilon_{\mu\nu} = \varepsilon_\nu^{(f)} - \varepsilon_\mu^{(i)} = (\varepsilon_\nu - \varepsilon_{\nu=0}) - (\varepsilon_\mu - \varepsilon_{\mu=0}) + eE^0$ is the difference in intrinsic free energy between the initial and final vibronic

states of the PCET reaction. By rearranging Eq. (26), we arrive at an expression consistent with our earlier derivations,

$$\Delta G_{\mu\nu}(\varepsilon,\eta) = e\eta + \Delta U_{\mu\nu} - (\varepsilon - E_F), \tag{27}$$

where $\Delta U_{\mu\nu} = (\varepsilon_\nu - \varepsilon_{\nu=0}) - (\varepsilon_\mu - \varepsilon_{\mu=0})$ is the intrinsic energy bias. By modifying the rate of electron transfer dependent on the position of the energy level ε given by Marcus in Eqs. (20) and (21), we arrive at

$$R_{r,\varepsilon}(\varepsilon,\eta) = \frac{k_0 c_O \rho_F}{\gamma_{TS}} \sum_\mu P_\mu \sum_\nu w_{\mu\nu}(\varepsilon,\eta), \tag{28}$$

$$R_{o,\varepsilon}(\varepsilon,\eta) = \frac{k_0 c_R \rho_F}{\gamma_{TS}} \sum_\nu P_\nu \sum_\nu w_{\nu\mu}(\varepsilon,\eta), \tag{29}$$

where k_0 satisfies microscopic reversibility,[37,39] ρ_F is the density of states at the Fermi level of the metallic phase, $P_{\mu/\nu}$ is the Boltzmann population of the vibronic state μ/ν given by the equation, and γ_{TS} is the activity coefficient of the transition state.[32] All vibrational information contained in the partial transition probability, $w_{ij}(\varepsilon,\eta)$, of a given pair of initial (i) and final (f) proton vibrational states at high temperatures closely resembles the nonadiabatic expression for ET given in Eqs. (17) and (18),[57,67]

$$w_{\mu\nu}(\varepsilon,\eta) = \frac{1}{\hbar}|V_{\mu\nu}|^2 \sqrt{\frac{\pi}{\lambda k_B T}} \exp\left(-\frac{(\lambda + e\eta_f + \Delta U_{\mu\nu} - (\varepsilon - E_F))^2}{4\lambda k_B T}\right), \tag{30}$$

$$w_{\nu\mu}(\varepsilon,\eta) = \frac{1}{\hbar}|V_{\mu\nu}|^2 \sqrt{\frac{\pi}{\lambda k_B T}} \exp\left(-\frac{(\lambda - e\eta_f - \Delta U_{\mu\nu} + (\varepsilon - E_F))^2}{4\lambda k_B T}\right). \tag{31}$$

The vibronic couplings $V_{\mu\nu}$ defines the interaction between reactant and product vibronic states in the diabatic representation of the PCET reaction. The vibronic states are defined by the electronic states and proton vibrational states. One justification for a nonadiabatic model is that the proton vibrational wavefunction overlap between reactant and product states is typically small for PCET reactions.[57] When the free electron involved in the RedOx reaction comes from/goes into a metallic phase, the rate of PCET dependent on the position of the energy level ε is expressed by combining Eqs. (28) and (29) with Eqs. (30) and (31),[47,74]

$$R_{r,\varepsilon}(\varepsilon,\eta) = \frac{k_0 c_O \rho_F \Lambda_\nu}{\gamma_{TS}\hbar} \sqrt{\frac{\pi}{\lambda k_B T}} \exp\left(-\frac{(\lambda + e\eta_f - (\varepsilon - E_F))^2}{4\lambda k_B T}\right) f(\varepsilon), \tag{32}$$

$$R_{o,\varepsilon}(\varepsilon,\eta) = \frac{k_0 c_R \rho_F \Lambda_\mu}{\gamma_{TS}\hbar} \sqrt{\frac{\pi}{\lambda k_B T}} \times \exp\left(-\frac{(\lambda - e\eta_f + (\varepsilon - E_F))^2}{4\lambda k_B T}\right)(1 - f(\varepsilon)), \tag{33}$$

where $\Delta\tilde{U}_{\mu\nu} = \Delta U_{\mu\nu}/k_B T$ and $\Lambda_\nu = \sum_{\mu,\nu} P_\nu |V_{\mu\nu}|^2 e^{-\Delta\tilde{U}_{\mu\nu}}$ and $\Lambda_\mu = \sum_{\mu,\nu} P_\mu |V_{\mu\nu}|^2 e^{\Delta\tilde{U}_{\mu\nu}}$ represent the summation over the vibronic states, vibronic couplings, and intrinsic energy bias between states for the reduction and oxidation reactions, respectively.[39] If the free electron involved in the RedOx reaction comes from a polaronic state, the density of states can be approximated by a Dirac delta function around the localized energy level ε_0; Eqs. (32) and (33) become[39]

$$R_r(\eta) = \frac{k_0 c_O c_e \Lambda_\nu}{\gamma_{TS}\hbar} \sqrt{\frac{\pi}{\lambda k_B T}} \exp\left(-\frac{(\lambda + e\eta_f)^2}{4\lambda k_B T}\right), \tag{34}$$

$$R_o(\eta) = \frac{k_0 c_R \Lambda_\mu}{\gamma_{TS}\hbar} \sqrt{\frac{\pi}{\lambda k_B T}} \exp\left(-\frac{(\lambda - e\eta_f)^2}{4\lambda k_B T}\right). \tag{35}$$

This expression gives the "inverted region" derived by Marcus when plotting the current–voltage relationships.[32,71] This limit is also discussed by Fraggedakis *et al.* for CIET with the key difference being the summation over mixed electron–proton vibronic states.[39]

C. PCET at the CeO_2–H_2/H_2O interface

The water electrolysis reaction (described in Table I) can be split into two steps at the CeO_2–H_2/H_2O interface plus the net result of the two reactions,

$$R_1: \ H_2O_{(g)} + V_O^{\cdot\cdot} + O_O^x \rightleftharpoons 2OH_O^{\cdot}, \tag{36}$$

$$R_2: \ 2OH_O^{\cdot} + 2Ce_{Ce}' \rightleftharpoons H_{2(g)} + 2O_O^x + +2Ce_{Ce}^x, \tag{37}$$

$$R_{o/r}: \ H_2O_{(g)} + V_O^{\cdot\cdot} + 2Ce_{Ce}' \rightleftharpoons H_{2(g)} + O_O^x + 2Ce_{Ce}^x, \tag{38}$$

where R_1 and R_2 represent the ion transfer (or water adsorption) and PCET reactions, respectively, and $R_{o/r}$ is the net chemical reaction. The affinities of the above three reactions are[37]

$$A_1 = 2\mu_{OH_O^{\cdot}} - \mu_{H_2O_{(g)}} - \mu_{V_O^{\cdot\cdot}} - \mu_{O_O^x}, \tag{39}$$

$$A_2 = \mu_{H_{2(g)}} + 2\mu_{O_O^x} + 2\mu_{Ce_{Ce}^x} - 2\mu_{OH_O^{\cdot}} - 2\mu_{Ce_{Ce}'}, \tag{40}$$

$$A_{r,o} = \mu_{H_{2(g)}} + 2\mu_{O_O^x} + 2\mu_{Ce_{Ce}^x} - \mu_{H_2O_{(g)}} - \mu_{V_O^{\cdot\cdot}} - 2\mu_{Ce_{Ce}'}, \tag{41}$$

where $A_{r,o}$ is the affinity of the net reaction. Since the adsorption step (R_1) is fast relative to the PCET step and in a state of quazi-equilibrium, we assume $A_1 = 0$ and $A_2 = A_{r,o}$ (derivation in the supplementary material). To calculate the concentration of surface species and the electrostatic surface potential as a function of overpotential, Eqs. (40) and (41) can be expanded,

$$\eta = E_2^{0'} + \frac{k_B T}{e} \ln\left(\frac{c_{O_O^x} c_{Ce_{Ce}^x} \sqrt{p_{H_{2(g)}}}}{c_{OH_O^{\cdot}} c_{Ce_{Ce}'}}\right) + \chi, \tag{42}$$

$$\eta = E^{0'} + \frac{k_B T}{2e} \ln\left(\frac{c_{O_O^x} c_{Ce_{Ce}^x}^{\ 2} p_{H_{2(g)}}}{c_{V_O^{\cdot\cdot}} c_{Ce_{Ce}'}^{\ 2} p_{H_2O_{(g)}}}\right), \tag{43}$$

where $E^{0'} = E_1^{0'} + E_2^{0'}$.[38] Equation (42) was conditioned to experimental data in Fig. 3(a), showing an exponential overpotential dependency on polaron concentration; Eq. (43) was conditioned

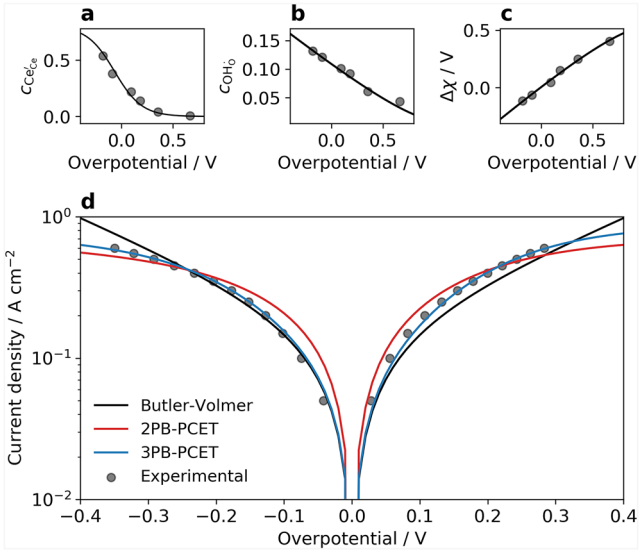

FIG. 3. (a) Polaron coverage, (b) hydroxyl coverage, and (c) electrostatic surface potential shift on a $Sm_{0.2}Ce_{0.8}O_{1.9}$–gas interface as a function of reservoir potential at 500 °C in 1:8:4 H_2O : H_2 : Ar. Gray circles represent data collected by APXPS measurements (Feng *et al*).[10] Polaron coverage is fit to Eq. (43); hydroxyl coverage and electrostatic surface potential shift is fit to Eq. (42).[1] (d) Current density as a function of overpotential for the Ni/CGO electrode in full cell (0.5 bar H_2, 0.5 bar H_2O, 600 °C). Gray circles represent experimentally observed current densities derived from electrochemical impedance spectroscopy (Williams *et al.*),[78] black lines represent the Butler–Volmer model given by Eq. (14) (RMSE = 0.166), red lines represent the 2PB-PCET model given by Eq. (44) (RMSE = 0.213), and blue lines represent the 3PB-PCET model given by Eq. (47) (RMSE = 0.074).

to experimental data in Figs. 3(a) and 3(b), illustrating a linear overpotential dependency on hydroxyl concentration and surface potential.[1,16] If the electron involved in the RedOx reaction at the MIEC–gas interface was polaronic, we do not integrate over the band structure of the metallic phase. As such, we can derive the solution for the rate of PCET at MIEC–gas interfaces via the 2 PB,

$$R_{r,o}^{2PB}(\eta) = \frac{k_0(1-\mathrm{x})^2}{\hbar}\sqrt{\frac{\pi}{\lambda k_B T}} \times \left(\frac{c_{Ce'_{Ce}} c_{OH^{\cdot}_O}}{c^{gas-eq}_{Ce'_{Ce}} c^{gas-eq}_{OH^{\cdot}_O}} \Lambda_\nu \exp\left(-\frac{(\lambda + e\Delta\chi)^2}{4\lambda k_B T}\right) - \frac{c_{Ce^x_{Ce}} c_{O^x_O}}{c^{gas-eq}_{Ce^x_{Ce}} c^{gas-eq}_{O^x_O}} \Lambda_\mu \exp\left(-\frac{(\lambda - e\Delta\chi)^2}{4\lambda k_B T}\right)\right). \quad (44)$$

When conditioning Eq. (44) to the electrochemical data on Fig. 3(d), we find a poor fitting. For the water reduction reaction at the 3 PB, the free electron involved in the PCET step comes from the metallic phase at an energy equal to, or below, the Fermi energy. As such, the rate of PCET at the Ni/CGO 3 PB (R^{3PB}) can be derived from Eqs. (32) and (33). By taking the equilibrium concentration outside the integral, the electrostatic surface potential shift is isolated according to Eq. (12),

$$R_r^{3PB}(\varepsilon,\eta) = \frac{\tilde{k}_0\Lambda_\nu}{\gamma_{TS}} \frac{c_{Ce'_{Ce}} c_{OH^{\cdot}_O}}{c^{gas-eq}_{Ce'_{Ce}} c^{gas-eq}_{OH^{\cdot}_O}} \times \int_{-\infty}^{\infty} \exp\left(-\frac{(\lambda + e\Delta\chi - (\varepsilon - E_F))^2}{4\lambda k_B T}\right) f(\varepsilon)\mathrm{d}\varepsilon, \quad (45)$$

$$R_o^{3PB}(\varepsilon,\eta) = \frac{\tilde{k}_0\Lambda_\mu}{\gamma_{TS}} \frac{c_{Ce^x_{Ce}} c_{O^x_O}}{c^{gas-eq}_{Ce^x_{Ce}} c^{gas-eq}_{O^x_O}} \times \int_{-\infty}^{\infty} \exp\left(-\frac{(\lambda - e\Delta\chi + (\varepsilon - E_F))^2}{4\lambda k_B T}\right)(1 - f(\varepsilon))\mathrm{d}\varepsilon, \quad (46)$$

where $\tilde{k}_0 = \frac{k_0\rho_F}{\hbar}\sqrt{\frac{\pi}{\lambda k_B T}}$. Equations (45) and (46) are shown to obey the De Donder relation in the supplementary material. The integrals given in Eqs. (45) and (46) are expressed analytically using the work of Zeng *et al.* to give the final solution for the rate of PCET at MIEC–gas interfaces via the 3 PB,[63]

$$R_{r,o}^{3PB}(\eta) = \tilde{k}_0(1-\mathrm{x})\left(\frac{c_{Ce'_{Ce}} c_{OH^{\cdot}_O}}{c^{gas-eq}_{Ce'_{Ce}} c^{gas-eq}_{OH^{\cdot}_O}} \frac{\Lambda_\nu}{1+e^{\Delta\tilde{\chi}}} - \frac{c_{Ce^x_{Ce}} c_{O^x_O}}{c^{gas-eq}_{Ce^x_{Ce}} c^{gas-eq}_{O^x_O}} \frac{\Lambda_\mu}{1+e^{-\Delta\tilde{\chi}}} \right) \times \mathrm{erfc}\left(\frac{\tilde{\lambda} - \sqrt{1+\tilde{\lambda}+\Delta\tilde{\chi}^2}}{2\sqrt{\tilde{\lambda}}}\right). \quad (47)$$

The transition states requires a Ce atom to occupy the cation site at the 3 PB. Therefore, we can express the activity coefficient of the transition state as $\gamma_{TS} = (1-\mathrm{x})^{-1}$, where x is the concentration of aliovalent dopants since the dopants cannot participate in RedOx reactions.[39] When conditioning Eq. (47) to the electrochemical impedance spectroscopy data, we find an excellent fit in Fig. 3(d). When compared to the Butler–Volmer equation [Eq. (14)] and 2PB-PCET equation [Eq. (44)], we find that the 3PB-PCET model fits the experimental data far better. This suggests that the mechanism involves PCET at the 3 PB and that the kinetics of this PCET reaction can be accurately captured using a nonadiabatic model. It is important to note that the vibronic coupling and Boltzmann population are difficult to calculate. Goldsmith *et al.* illustrated limited change in the contribution from each vibronic coupling relative to the exponentially scaled electrostatic component.[75] Therefore, we assume that we do not observe their effects in the current–voltage experiment. From this fitting, we were able to calculate the reorganization energy $\lambda = 18k_BT$ (1.35 eV at 873 K). This is large relative to that estimated for lithium ion intercalation into $LiFePO_4$ ($\lambda_{LiFePO_4} = 8.3k_BT$) and graphite ($\lambda_{LiC_6} = 5k_BT$).[31,76] DFT calculations carried out by Castleton *et al.* approximated the diabatic barrier for polaron migration in bulk $CeO_{2-\delta}$.[77] The result that agreed closest to our system was the local density approximation + U (LDA + U), which yielded $\lambda_{LDA+U} = 1.28$ eV. However, there was a wide range of results as the barrier was heavily dependent on the functional used; moreover, the

polaron migration process is not entirely representative of the PCET process.

Interesting, the electrostatic driving force in Eqs. (47) and (44) is the electrostatic surface potential located at the MIEC–gas interface, even if the PCET event occurs at the 3 PB.[2] The origin of this phenomenon is rooted in the dipole–dipole interactions, whereby the coverage of adsorbates at the 3 PB will influence the adsorption thermodynamics across the MIEC–gas interface. Under water electrolysis mode, PCET is driven by the charged particles (adsorbates and polarons) seeking to establish thermodynamic equilibrium with the gas phase, resulting in the release of hydrogen, relaxation of the electrostatic surface potential, and a spatial region free of charged particles. When PCET occurs at the 2 PB, a charge-free region will be filled as the charged particles reorganize to maximize configurational entropy and minimize columbic interactions. The same principle applies to the 3 PB mechanism, where a charge-free region close to the 3 PB will stimulate reorganization across the entire MIEC surface, resulting in the relaxation of the electrostatic surface potential at the CeO_2–H_2/H_2O interface. We can account for the asymmetry observed in the current–voltage plot in Fig. 3(d) to dipole–dipole depolarization. This occurs when a dipole is exposed to the electrostatic field of all other dipoles, shrinking in the hydroxyl bond length, thereby reducing the size of the electric field normal to the surface. Dipole–dipole depolarization increased at negative overpotential as the coverage of hydroxyls on the electrode surface increases [Fig. 3(b)].[1,2,16] A decrease in the adsorbate dipole moment reduces the magnitude of the surface potential shift and therefore increases the resistance of the PCET process at negative overpotentials relative to positive overpotentials.

IV. CONCLUSION

In this work, the origin and physics of the activation overpotential for the Ni/CGO fuel electrode has been explained. Previously, we demonstrated the effects of nonequilibrium thermodynamics on the concentration of electronic defects and the adsorbate induced electrostatic surface potential. Here, we derive a kinetic relationship between the overpotential and surface potential via the 2 and 3 PB mechanism. In the framework of the proton-coupled electron transfer (PCET) theory, electronic and protonic species were treated as quantum particles whereby the probability of a concerted tunneling event was controlled by an external voltage. To account for the electronic structure of the metallic phase, variation in the density of states was neglected to give an analytical expression for the hydrolysis reaction via the 3 PB. Using the current–voltage data, we found the best fit was given by the 3 PB PCET equation vs the Butler–Volmer equation and the 2 PB PCET equation. This suggested that the dominant pathway for charge transfer at the Ni/CGO electrode includes the electrocatalytic metallic phase. Understanding the mechanism of ambipolar charge transfer at the electrode–gas interface is a significant consideration for the design and operational conditions of SOC electrodes as the strength of the intrinsic dipole moment of the adsorbed gas species is shown to have a profound effect on the magnitude of the activation overpotential. The theory of the electrostatic surface potential put forward in this work is not confined to PCET processes at SOFC electrodes and can be extended to other fields where charge transfer occurs at a solid–gas interface, such as nitrogen reduction and in lithium air batteries.

SUPPLEMENTARY MATERIAL

Supplementary material notes: derivations of the electrostatic surface potential, affinity of the water electrolysis reaction, and the de Donder relation.

ACKNOWLEDGMENTS

This work was supported by Ceres Power Ltd. I.D.S. and S.J.S. acknowledge the EPSRC for funding through the award of Grant No. EP/R002010/1. R.E.W. acknowledges start-up funding from the Case School of Engineering at Case Western Reserve University.

AUTHOR DECLARATIONS

Conflict of Interest

The authors have no conflicts to disclose.

Author Contributions

Nicholas J. Williams: Conceptualization (lead); Data curation (lead); Methodology (lead); Writing – original draft (lead). **Robert E. Warburton**: Formal analysis (supporting); Validation (supporting); Writing – review & editing (supporting). **Ieuan D. Seymour**: Visualization (supporting); Writing – original draft (supporting); Writing – review & editing (supporting). **Alexander E. Cohen**: Visualization (supporting); Writing – original draft (supporting); Writing – review & editing (supporting). **Martin Z. Bazant**: Supervision (equal); Writing – review & editing (supporting). **Stephen J. Skinner**: Supervision (equal).

DATA AVAILABILITY

The data that support the findings of this study are available within the article and its supplementary material.

REFERENCES

[1] N. J. Williams, I. D. Seymour, R. T. Leah, S. Mukerjee, M. Selby, and S. J. Skinner, "Theory of the electrostatic surface potential and intrinsic dipole moments at the mixed ionic electronic conductor (MIEC)–gas interface," Phys. Chem. Chem. Phys. **23**, 14569–14579 (2021).

[2] N. J. Williams, I. D. Seymour, R. T. Leah, A. Banerjee, S. Mukerjee, and S. J. Skinner, "Non-equilibrium thermodynamics of mixed ionic-electronic conductive electrodes and their interfaces: A Ni/CGO study," J. Mater. Chem. A **10**, 11121–11130 (2022).

[3] S. Skinner and M. Laguna-Bercero, "Advanced inorganic materials for solid oxide fuel cells," in Energy Materials, edited by D. W. Bruce, D. O'Hare, and R. I. Walton (Wiley, 2011), pp. 33–94.

[4] Z. Guan, D. Chen, and W. C. Chueh, "Analyzing the dependence of oxygen incorporation current density on overpotential and oxygen partial pressure in mixed conducting oxide electrodes," Phys. Chem. Chem. Phys. **19**, 23414–23424 (2017).

[5] S. Dierickx, A. Weber, and E. Ivers-Tiffée, "How the distribution of relaxation times enhances complex equivalent circuit models for fuel cells," Electrochim. Acta **355**, 136764 (2020).

[6] A. Nenning, A. K. Opitz, C. Rameshan, R. Rameshan, R. Blume, M. Hävecker, A. Knop-Gericke, G. Rupprechter, B. Klötzer, and J. Fleig, "Ambient pressure

XPS study of mixed conducting perovskite-type SOFC cathode and anode materials under well-defined electrochemical polarization," J. Phys. Chem. C **120**, 1461–1471 (2016).
[7]A. Schmid and J. Fleig, "The current-voltage characteristics and partial pressure dependence of defect controlled electrochemical reactions on mixed conducting oxides," J. Electrochem. Soc. **166**, F831–F846 (2019).
[8]H. A. Hansen and C. Wolverton, "Kinetics and thermodynamics of H_2O dissociation on reduced CeO_2(111)," J. Phys. Chem. C **118**, 27402–27414 (2014).
[9]Z. Cheng, B. J. Sherman, and C. S. Lo, "Carbon dioxide activation and dissociation on ceria (110): A density functional theory study," J. Chem. Phys. **138**, 014702 (2013).
[10]Z. A. Feng, C. Balaji Gopal, X. Ye, Z. Guan, B. Jeong, E. Crumlin, and W. C. Chueh, "Origin of overpotential-dependent surface dipole at CeO_{2-x}/Gas interface during electrochemical oxygen insertion reactions," Chem. Mater. **28**, 6233–6242 (2016).
[11]S. Wang, T. Kobayashi, M. Dokiya, and T. Hashimoto, "Electrical and ionic conductivity of Gd-doped ceria," J. Electrochem. Soc. **147**, 3606 (2000).
[12]S. Grieshammer, B. O. H. Grope, J. Koettgen, and M. Martin, "A combined DFT + U and Monte Carlo study on rare earth doped ceria," Phys. Chem. Chem. Phys. **16**, 9974–9986 (2014).
[13]S. Grieshammer, M. Nakayama, and M. Martin, "Association of defects in doped non-stoichiometric ceria from first principles," Phys. Chem. Chem. Phys. **18**, 3804–3811 (2016).
[14]D. Van Laethem, J. Deconinck, and A. Hubin, "Multiscale modeling of the ionic conductivity of acceptor doped ceria," J. Eur. Ceram. Soc. **40**, 2404–2416 (2020).
[15]M. Kishimoto, M. Lomberg, E. Ruiz-Trejo, and N. P. Brandon, "Numerical modeling of nickel-infiltrated gadolinium-doped ceria electrodes reconstructed with focused ion beam tomography," Electrochim. Acta **190**, 178–185 (2016).
[16]N. J. Williams, I. D. Seymour, D. Fraggedakis, and S. J. Skinner, "Electric fields and charge separation for solid oxide fuel cell electrodes," Nano Lett. **22**, 7515 (2022).
[17]A. Nenning, C. Bischof, J. Fleig, M. Bram, and A. K. Opitz, "The relation of microstructure, materials properties and impedance of SOFC electrodes: A case study of Ni/GDC Anodes," Energies **13**, 987 (2020).
[18]M. C. Doppler, J. Fleig, M. Bram, and A. K. Opitz, "Hydrogen oxidation mechanisms on Ni/yttria stabilized zirconia anodes: Separation of reaction pathways by geometry variation of pattern electrodes," J. Power Sources **380**, 46–54 (2018).
[19]A. Nenning, M. Holzmann, J. Fleig, and A. K. Opitz, "Excellent kinetics of single-phase Gd-doped ceria fuel electrodes in solid oxide cells," Mater. Adv. **2**, 5422–5431 (2021).
[20]K. Yamaji, N. Sakai, M. Ishikawa, H. Yokokawa, and M. Dokiya, "Electrode reaction at platinum/ceria surface modified YSZ interface," Ionics **3**, 67–74 (1997).
[21]H. Yokokawaa and T. Kawadab, "Characterization of ceria coated YSZ by a platinum point electrode in H_2-H_2O atmosphere," Solid State Ionics **2738**, 1259–1266 (1996).
[22]N. Sakai, K. Yamaji, T. Horita, H. Kishimoto, Y. P. Xiong, and H. Yokokawa, "Significant effect of water on surface reaction and related electrochemical properties of mixed conducting oxides," Solid State Ionics **175**, 387–391 (2004).
[23]M. Brown, S. Primdahl, and M. Mogensen, "Structure/performance relations for Ni/Yttria-stabilized zirconia anodes for solid oxide fuel cells," J. Electrochem. Soc. **147**, 475 (2000).
[24]S. P. Jiang and S. P. S. Badwal, "Hydrogen oxidation at the nickel and platinum electrodes on yttria-tetragonal zirconia electrolyte," J. Electrochem. Soc. **144**, 3777 (1997).
[25]H. Yokokawa, T. Horita, N. Sakai, K. Yamaji, M. Brito, Y. Xiong, and H. Kishimoto, "Protons in ceria and their roles in SOFC electrode reactions from thermodynamic and SIMS analyses," Solid State Ionics **174**, 205–221 (2004).
[26]A. Bieberle and L. J. Gauckler, "Reaction mechanism of Ni pattern anodes for solid oxide fuel cells," Solid State Ionics **135**, 337–345 (2000).
[27]T. Horita, H. Kishimoto, K. Yamaji, Y. Xiong, N. Sakai, M. Brito, and H. Yokokawa, "Materials and reaction mechanisms at anode/electrolyte interfaces for SOFCs," Solid State Ionics **177**, 1941–1948 (2006).
[28]W. G. Bessler, S. Gewies, and M. Vogler, "A new framework for physically based modeling of solid oxide fuel cells," Electrochim. Acta **53**, 1782–1800 (2007).
[29]S. Primdahl and M. Mogensen, "Oxidation of hydrogen on Ni/YSZ cermet Anodes.pdf," J. Electrochem. Soc. **144**, 3409–3419 (1997).
[30]J. H. Nam and D. H. Jeon, "A comprehensive micro-scale model for transport and reaction in intermediate temperature solid oxide fuel cells," Electrochim. Acta **51**, 3446–3460 (2006).
[31]P. Bai and M. Z. Bazant, "Charge transfer kinetics at the solid-solid interface in porous electrodes," Nat. Commun. **5**, 3585 (2014).
[32]M. Z. Bazant, "Theory of chemical kinetics and charge transfer based on nonequilibrium thermodynamics," Acc. Chem. Res. **46**, 1144–1160 (2013).
[33]J. Fleig and J. Jamnik, "Work function changes of polarized electrodes on solid electrolytes," J. Electrochem. Soc. **152**, E138 (2005).
[34]S. Hammes-Schiffer, "Theoretical perspectives on proton-coupled electron transfer reactions," Acc. Chem. Res. **34**, 273–281 (2001).
[35]S. Hammes-Schiffer and A. V. Soudackov, "Proton-coupled electron transfer in solution, proteins, and electrochemistry," J. Phys. Chem. B **112**, 14108–14123 (2008).
[36]S. Hammes-Schiffer, "Introduction: Proton-coupled electron transfer," Chem. Rev. **110**, 6937–6938 (2010).
[37]D. Kondepudi and I. Prigogine, *Modern Thermodynamics: From Heat Engines to Dissipative Structures* (John Wiley & Sons, 2014).
[38]A. J. Bard, L. R. Faulkner, and H. S. White, *Electrochemical Methods: Fundamentals and Applications* (John Wiley & Sons, 2022).
[39]D. Fraggedakis, M. McEldrew, R. B. Smith, Y. Krishnan, Y. Zhang, P. Bai, W. C. Chueh, Y. Shao-Horn, and M. Z. Bazant, "Theory of coupled ion-electron transfer kinetics," Electrochim. Acta **367**, 137432 (2021).
[40]S. R. Kelly, C. Kirk, K. Chan, and J. K. Nørskov, "Electric field effects in oxygen reduction kinetics: Rationalizing ph dependence at the Pt(111), Au(111), and Au(100) electrodes," J. Phys. Chem. C **124**, 14581–14591 (2020).
[41]W. Lai and F. Ciucci, "Mathematical modeling of porous battery electrodes-Revisit of Newman's model," Electrochim. Acta **56**, 4369–4377 (2011).
[42]M. Z. Bazant, "Thermodynamic stability of driven open systems and control of phase separation by electro-autocatalysis," Faraday Discuss. **199**, 423–463 (2017).
[43]R. Rao and M. Esposito, "Nonequilibrium thermodynamics of chemical reaction networks: Wisdom from stochastic thermodynamics," Phys. Rev. X **6**, 041064 (2016).
[44]C. B. Gopal, F. E. Gabaly, A. H. McDaniel, and W. C. Chueh, "Origin and tunability of unusually large surface capacitance in doped cerium oxide studied by ambient-pressure X-ray photoelectron spectroscopy," Adv. Mater. **28**, 4692–4697 (2016).
[45]J. Fleig, "On the current-voltage characteristics of charge transfer reactions at mixed conducting electrodes on solid electrolytes," Phys. Chem. Chem. Phys. **7**, 2027–2037 (2005).
[46]J. Fleig, R. Merkle, and J. Maier, "The $p(O_2)$ dependence of oxygen surface coverage and exchange current density of mixed conducting oxide electrodes: Model considerations," Phys. Chem. Chem. Phys. **9**, 2713–2723 (2007).
[47]D. Fraggedakis and M. Z. Bazant, "Tuning the stability of electrochemical interfaces by electron transfer reactions," J. Chem. Phys. **152**, 184703 (2020).
[48]M. C. Henstridge, E. Laborda, N. V. Rees, and R. G. Compton, "Marcus-hush-chidsey theory of electron transfer applied to voltammetry: A review," Electrochim. Acta **84**, 12–20 (2012).
[49]W. Dreyer, C. Guhlke, and R. Müller, "A new perspective on the electron transfer: Recovering the Butler-Volmer equation in non-equilibrium thermodynamics," Phys. Chem. Chem. Phys. **18**, 24966–24983 (2016).
[50]A. J. Bard, M. Stratmann, and E. Calvo, "Interfacial kinetics and mass transport," in *Encyclopedia of Electrochemistry* (Wiley-VCH, 2003), Vol. 2.
[51]S. Fletcher, "Tafel slopes from first principles," J. Solid State Electrochem. **13**, 537–549 (2009).
[52]N. A. Deskins and M. Dupuis, "Electron transport via polaron hopping in bulk Ti O_2: A density functional theory characterization," Phys. Rev. B **75**, 1–10 (2007).
[53]S. Fletcher, "The theory of electron transfer," J. Solid State Electrochem. **14**, 705–739 (2010).

[54]Z. Albert Feng, "Operando X-ray photoelectron spectroscopy investigation of ceria/gas electrochemical interfaces,", Ph.D. thesis, Stanford University, 2015, pp. 1–141.
[55]R. B. Smith and M. Z. Bazant, "Multiphase porous electrode theory," J. Electroche. Soc. **164**, E3291–E3310 (2017).
[56]Y. Zeng, R. B. Smith, P. Bai, and M. Z. Bazant, "Simple formula for Marcus-Hush-Chidsey kinetics," J. Electroanal. Chem. **735**, 77–83 (2014).
[57]R. E. Warburton, A. V. Soudackov, and S. Hammes-Schiffer, "Theoretical modeling of electrochemical proton-coupled electron transfer," Chem. Rev. **122**, 10599 (2022).
[58]R. Dogonadze, A. Kuznetsov, and M. Vorotyntsev, "The kinetics of the adiabatic and nonadiabatic reactions at the metal and semiconductor electrodes," Croat. Chem. Acta **44**, 257–273 (1972).
[59]R. R. Dogonadze, A. M. Kuznetsov, and M. A. Vorotyntsev, "On the theory of adiabatic and non-adiabatic electrochemical reactions," J. Electroanal. Chem. Interfacial Electrochem. **25**, A17–A19 (1970).
[60]K. Saito and H. Sumi, "Unified expression for the rate constant of the bridged electron transfer derived by renormalization," J. Chem. Phys. **131**, 134101 (2009).
[61]B. Hammer and J. K. Nørskov, "Electronic factors determining the reactivity of metal surfaces," Surf. Sci. **343**, 211–220 (1995).
[62]A. Soudackov and S. Hammes-Schiffer, "Multistate continuum theory for multiple charge transfer reactions in solution," J. Chem. Phys. **111**, 4672–4687 (1999).
[63]D. R. Weinberg, C. J. Gagliardi, J. F. Hull, C. F. Murphy, C. A. Kent, B. C. Westlake, A. Paul, D. H. Ess, D. G. McCafferty, and T. J. Meyer, "Proton-coupled electron transfer," Chem. Rev. **112**, 4016–4093 (2012).
[64]P. Goyal, C. A. Schwerdtfeger, A. V. Soudackov, and S. Hammes-Schiffer, "Nonadiabatic dynamics of photoinduced proton-coupled electron transfer in a solvated phenol–amine complex," J. Phys. Chem. B **119**, 2758–2768 (2015).
[65]A. Hazra, A. V. Soudackov, and S. Hammes-Schiffer, "Role of solvent dynamics in ultrafast photoinduced proton-coupled electron transfer reactions in solution," J. Phys. Chem. B **114**, 12319–12332 (2010).
[66]M. K. Ludlow, J. H. Skone, and S. Hammes-Schiffer, "Substituent effects on the vibronic coupling for the phenoxyl/phenol self-exchange reaction," J. Phys. Chem. B **112**, 336–343 (2008).
[67]C. Venkataraman, A. V. Soudackov, and S. Hammes-Schiffer, "Theoretical formulation of nonadiabatic electrochemical proton-coupled electron transfer at metal-solution interfaces," J. Phys. Chem. C **112**, 12386–12397 (2008).
[68]D. G. Nocera, "Proton-coupled electron transfer: The engine of energy conversion and storage," J. Am. Chem. Soc. **144**, 1069–1081 (2022).
[69]J. W. Darcy, B. Koronkiewicz, G. A. Parada, and J. M. Mayer, "A continuum of proton-coupled electron transfer reactivity," Acc. Chem. Res. **51**, 2391–2399 (2018).
[70]R. G. Agarwal, S. C. Coste, B. D. Groff, A. M. Heuer, H. Noh, G. A. Parada, C. F. Wise, E. M. Nichols, J. J. Warren, and J. M. Mayer, "Free energies of proton-coupled electron transfer reagents and their applications," Chem. Rev. **122**, 1–49 (2021).
[71]R. A. Marcus, "On the theory of electron-transfer reactions. VI. Unified treatment for homogeneous and electrode reactions," J. Chem. Phys. **43**, 679–701 (1965).
[72]G. Chen, *Nanoscale Energy Transport and Conversion: A Parallel Treatment of Electrons, Molecules, Phonons, and Photons* (Oxford University Press, 2005).
[73]A. M. Kuznetsov and J. Ulstrup, *Electron Transfer in Chemistry and Biology: An Introduction to the Theory* (John Wiley & Sons Ltd, 1999).
[74]Y. Zeng, P. Bai, R. B. Smith, and M. Z. Bazant, "Simple formula for asymmetric Marcus-Hush kinetics," J. Electroanal. Chem. **748**, 52–57 (2015).
[75]Z. K. Goldsmith, Y. C. Lam, A. V. Soudackov, and S. Hammes-Schiffer, "Proton discharge on a gold electrode from triethylammonium in acetonitrile: Theoretical modeling of potential-dependent kinetic isotope effects," J. Am. Chem. Soc. **141**, 1084–1090 (2018).
[76]T. Gao, Y. Han, D. Fraggedakis, S. Das, T. Zhou, C.-N. Yeh, S. Xu, W. C. Chueh, J. Li, and M. Z. Bazant, "Interplay of lithium intercalation and plating on a single graphite particle," Joule **5**, 393–414 (2021).
[77]C. W. M. Castleton, A. Lee, and J. Kullgren, "Benchmarking density functional theory functionals for polarons in oxides: Properties of CeO_2," J. Phys. Chem. C **123**, 5164–5175 (2019).
[78]N. J. Williams, C. Osborne, I. D. Seymour, M. Z. Bazant, and S. J. Skinner, "Application of finite Gaussian process distribution of relaxation times on SOFC electrodes," Electrochem. Commun. **2023**, 107458.